


Galaxy And Mass Assembly (GAMA): The absence of stellar mass segregation in galaxy groups and consistent predictions from GALFORM and EAGLE simulations

P. R. Kafle,¹  A. S. G. Robotham,¹ C. del P. Lagos,¹ L. J. Davies,¹ A. J. Moffett,¹ S. P. Driver,^{1,2} S. K. Andrews,¹ I. K. Baldry,³ J. Bland-Hawthorn,⁴ S. Brough,⁵ L. Cortese,¹ M. J. Drinkwater,⁶ R. Finnegan,¹ A. M. Hopkins⁵ and J. Loveday⁷

¹ ICRAR, The University of Western Australia, 35 Stirling Highway, Crawley, WA 6009, Australia

² SUPA, School of Physics & Astronomy, University of St Andrews, North Haugh, St Andrews KY16 9SS, UK

³ Astrophysics Research Institute, Liverpool John Moores University, IC2, Liverpool Science Park, 146 Brownlow Hill, Liverpool L3 5RF, UK

⁴ Sydney Institute for Astronomy, School of Physics A28, University of Sydney, NSW 2006, Australia

⁵ Australian Astronomical Observatory, PO Box 915, North Ryde, NSW 1670, Australia

⁶ Department of Physics, The University of Queensland, Brisbane, QLD 4072, Australia

⁷ Astronomy Centre, University of Sussex, Falmer, Brighton BN1 9QH, UK

9 March 2022

ABSTRACT

We investigate the contentious issue of the presence, or lack thereof, of satellites mass segregation in galaxy groups using the Galaxy And Mass Assembly (GAMA) survey, the GALFORM semi-analytic and the EAGLE cosmological hydrodynamical simulation catalogues of galaxy groups. We select groups with halo mass $12 \leq \log(M_{\text{halo}}/h^{-1}M_{\odot}) < 14.5$ and redshift $z \leq 0.32$ and probe the radial distribution of stellar mass out to twice the group virial radius. All the samples are carefully constructed to be complete in stellar mass at each redshift range and efforts are made to regularise the analysis for all the data. Our study shows negligible mass segregation in galaxy group environments with absolute gradients of $\lesssim 0.08$ dex and also shows a lack of any redshift evolution. Moreover, we find that our results at least for the GAMA data are robust to different halo mass and group centre estimates. Furthermore, the EAGLE data allows us to probe much fainter luminosities (r -band magnitude of 22) as well as investigate the three-dimensional spatial distribution with intrinsic halo properties, beyond what the current observational data can offer. In both cases we find that the fainter EAGLE data show a very mild spatial mass segregation at $z \leq 0.22$, which is again not apparent at higher redshift. Interestingly, our results are in contrast to some earlier findings using the Sloan Digital Sky Survey. We investigate the source of the disagreement and suggest that subtle differences between the group finding algorithms could be the root cause.

Key words: galaxies: evolution-formation - groups: general – galaxies: haloes

1 INTRODUCTION

Both theoretical modelling of galaxy formation and observations reveal that most of the stellar material in the Universe resides in groups of a few $10^{12}M_{\odot}$ and larger masses (e.g. Abell 1958; Rose 1977; Hickson 1982; Huchra & Geller 1982; Geller & Huchra 1983; Mulchaey 2000; Eke et al. 2004;

Berlind et al. 2006; Yang et al. 2007; Knobel et al. 2009; Robotham et al. 2011; Nurmi et al. 2013; Tempel et al. 2014; Le Brun et al. 2014; Saulder et al. 2015, etc). Moreover, it is known that galaxies residing in a group environment follow a very different evolutionary course compared to that of isolated systems (Einasto et al. 1974; Postman & Geller 1984). Therefore, the group environment is clearly an important factor in understanding both structure formation and galaxy evolution at intermediate local mass densities.

* E-mail: prajwal.kafle@uwa.edu.au, prrajkafe@gmail.com

In current galaxy formation models, galaxies in the groups can be broadly classified in two categories: central galaxies and satellite galaxies (e.g. Zheng et al. 2005; Skibba et al. 2011, etc). Central galaxies are located near the centre of a parent dark matter halo. Under the current paradigm of hierarchical structure formation, the central galaxies of the subhalo that gets accreted to the dominant nearby halo are called satellites. Subsequently the accreted galaxies (satellites) are potentially quenched by environmental effects, such as gas stripping by ram-pressure (Gunn & Gott 1972; Bekki 2009), removal or reduction of hot/cold gas or even the stellar components of the satellite galaxy due to tidal stripping (Moore et al. 1996; Boselli & Gavazzi 2006). Thus, to develop a viable theory of galaxy formation it is important to understand the processes that could influence the abundance and distribution of satellites in galaxy groups.

A spatial distribution of stellar mass segregation in any dynamical system, ranging from globular clusters to galaxy groups and clusters, is an important indicator of their evolutionary history and dynamical friction time-scales. The sinking of heavier objects in a gravitational potential well of stellar (Bonnell & Davies 1998) and galaxy (White 1977; Gao et al. 2004; McIntosh et al. 2005) clusters has been repeatedly observed. Broadly, the mass segregation is known to be either primordial (Bonnell et al. 1997), meaning clusters may form with the most massive galaxies concentrated near the centre, or dynamical (Allison et al. 2009) caused by migration of the most massive galaxies into the centre of the cluster via relaxation. If dynamical friction in the group environment plays a dominant role, then the effect on the stellar mass distribution in galaxy groups should be detectable. Conversely, if there is an absence of spatial mass segregation in groups, it could possibly mean that the contribution of ongoing star formation in galaxies, or tidal stripping of satellite galaxies as they fall inward, or that the group is continually fed by new merging groups in a dominant process directing the distribution of the mass in groups. In other words, it means that the relaxation time of the galaxy groups is significantly longer than their crossing time.

With the advent of large redshift surveys it has only recently become possible to study mass segregation in galaxy groups in great detail using the Sloan Digital Sky Survey (SDSS; York et al. 2000) and zCOSMOS (Knobel et al. 2012). Recently, Roberts et al. (2015) showed the presence of mass segregation trends in SDSS, meaning satellites of higher masses are systematically concentrated close to the group-centre at all halo mass ranges. This is in close agreement with earlier studies using different data sets, for example, van den Bosch et al. (2008, SDSS) and Presotto et al. (2012, zCOSMOS). Similarly, Balogh et al. (2014) also find some mass segregation, but at small group radii of $\lesssim 0.1$ times the virial radius. Simultaneously, there are also evidence to contradict the existence of mass segregations in galaxy groups. For example, Ziparo et al. (2013) fail to observe strong mass segregation in X-ray selected groups up to $z \sim 1.7$. However, they could not rule out that this might be due to a bias introduced by their sample selection. Similarly Wetzell et al. (2012), using galaxy group catalogues created from SDSS DR7, with a modified implementation of the group-finding algorithm in Yang et al. (2007), also find no evidence of mass segregation for satellites at any halo mass range.

Despite this large body of work, there is little consensus on the presence or the strength of mass segregation in galaxy groups. On the theory side there have been analogous studies (e.g. De Lucia et al. 2004; Reed et al. 2005; van den Bosch et al. 2016, etc) that show the segregation of dark matter subhaloes in numerical simulations of various extents, but also see Diemand et al. (2004); Springel et al. (2008); Ludlow et al. (2009) for contradictory findings. In the future, it would be valuable to combine the theoretical work with the studies of satellites mass segregation in galaxy groups to better understand the galaxy-halo connection and the various physical processes, such as how galaxies populate haloes.

In this work we aim to resolve the contentious issue of the presence or absence of mass segregation in galaxy groups. For this we investigate group catalogues from three types of data, observed: using the Galaxy and Mass Assembly survey (GAMA; Driver et al. 2011; Liske et al. 2015); semi-analytics: using the GAMA lightcone mock catalogues (GAMA-Mock; Merson et al. 2013 using the Gonzalez-Perez et al. (2014) variant of the GALFORM semi-analytic model of galaxy formation (Cole et al. 2000; Lacey et al. 2015)), and cosmological hydrodynamical simulation: using the Evolution and Assembly of GaLaxies and their Environments (EAGLE; Schaye et al. 2015; McAlpine et al. 2015). In order to make the results from all the three data sets comparable, we homogenise the estimates of physical quantities such as group-centric distance, stellar mass and halo virial properties.

Throughout the paper we assume a cosmological constant $\Omega_\Lambda = 0.75$, matter density $\Omega_M = 0.25$ and $h = H_0/(100 \text{ km s}^{-1} \text{ Mpc}^{-1})$. Also, \log stands for logarithm to the base 10, and r and R represent the spherical (3D) and projected (2D) radii respectively. For conciseness, we use the standard notation $($ and $)$ to denote open and closed intervals respectively.

This paper is arranged as follows. In Section 2, we describe GAMA, GAMA-Mock and EAGLE data, their corresponding group catalogues and the derivation of quantities relevant to our analysis. In Section 3 we present our main results. In Section 4 we provide a detailed comparison of our work with the available group catalogues of Sloan Digital Sky Survey (SDSS) data and also among different group catalogues of SDSS. Our findings are summarised in Section 5.

2 DATA

We use data from three main sources. We first describe the data sets individually followed by how we compute information relevant to the study of mass segregation within galaxy groups.

2.1 Galaxy and Mass Assembly (GAMA)

The GAMA survey is a spectroscopic and multiwavelength survey of galaxies carried out on the Anglo-Australian Telescope (Driver et al. 2011; Liske et al. 2015). Details of the GAMA survey characteristics are given in Driver et al. (2011), with the survey input catalogue described in Baldry

et al. (2010), the spectroscopic processing outlined in Hopkins et al. (2013), and the spectroscopic tiling algorithm explained in Robotham et al. (2010). The survey has obtained 300,000 galaxy redshifts to $r < 19.8$ mag over ~ 286 deg², with the survey design aimed at providing uniform spatial completeness (Baldry et al. 2010; Driver et al. 2011). Here we use the complete northern equatorial sample referred to as GAMA-II-N covering over three 12×5 deg² fields centred at 9^h(G09), 12^h(G12) and 14.5^h(G15) RA and approximately 0° declination, described in full in Liske et al. (2015).

The data used here primarily focusses on the GAMA galaxy groups, which are constructed using an adaptive Friends-of-Friends (FoF) algorithm, linking galaxies in projected and line-of-sight separations. For the full details about the algorithm, diagnostic tests, construction and caveats of the group catalogue we refer the reader to Robotham et al. (2011).

2.2 Semi-analytic Data (GAMA-Mock)

We use the GAMA light cone mock catalogues constructed from the GALFORM semi-analytic model of galaxy formation (Gonzalez-Perez et al. 2014). The model uses analytic, physically motivated equations to follow the evolution of the baryonic components of galaxies (stars, cold gas, hot gas, and their metals). GALFORM makes use of these equations to populate dark matter halo merger trees that are generated from N -body simulations (a new Millennium Simulation MS-W7; Guo et al. 2013) of dark matter. The MS-W7 simulation uses 2160^3 particles, each with a mass of $9.35 \times 10^8 h^{-1} M_\odot$ in a box of side $500 h^{-1}$ Mpc (see Springel et al. 2005, for details of the original Millennium Simulation).

GALFORM models the following processes in galaxies: (i) the collapse and merging of dark matter haloes, (ii) gas heating and cooling through shocks and radiative cooling inside dark matter haloes, leading to the formation of galactic disks, (iii) quiescent star formation in galactic disks, (iv) supernovae and AGN feedback from the photo-ionization of the intergalactic medium, (v) chemical enrichment of gas and stars, (vi) galaxy mergers leading to the formation of stellar spheroids, which can also trigger a starburst, and (vii) the collapse of gravitationally unstable disks, which also leads to the formation of spheroids and starbursts. The scale size of the disk and bulge of galaxies is also computed. The galaxy luminosities are determined by combining the star formation and metal enrichment histories with stellar population synthesis models for each galaxy. The attenuation of starlight by dust is included based on radiative transfer calculations. The final product of the calculation is a prediction of the number and properties of galaxies that reside within dark matter haloes of different masses. The model we use here is that of Gonzalez-Perez et al. (2014). The outputs of the model are placed in a lightcone using the technique described in Merson et al. (2013), and the details for how the GAMA selection and sky areas were applied to the lightcones are described in Farrow et al. (2015).

Importantly, the construction of the group catalogue for GAMA-Mock and estimates of the group properties, e.g., galaxy stellar mass, group centre and projected distance etc are done similar to the GAMA data. This effort is to ensure consistency and make GAMA and GAMA-Mock results comparable. However, Robotham et al. (2011) showed that

the main discrepancy between the observed GAMA group catalogue and the mock lightcone is that there is a relative excess of very compact groups in the mocks data otherwise there is a high degree of agreement between the two data sets.

2.3 EAGLE: a cosmological hydrodynamical simulation

The final data set that we compare to our observational results is taken from the Evolution and Assembly of GaLaxies and their Environments (EAGLE, Schaye et al. 2015) simulation. EAGLE is a suite of cosmological hydrodynamical simulations performed at a range of numerical resolutions, in periodic volumes with a range of sizes, and using a variety of subgrid implementations to model physical processes below the resolution limit. One of the unique aspects of EAGLE is the plethora of sub-grid baryonic physics included in the model: (i) radiative cooling and photoheating rates, (ii) star formation, (iii) stellar evolution and metal enrichment, (iv) stellar feedback, and (v) black hole growth and AGN feedback. These physical models are the key to reproducing a large set of properties of the observed galaxy population in the local Universe. For more details of the simulation we refer the reader to Schaye et al. (2015). The subgrid parameters of the EAGLE reference model are calibrated to the $z = 0$ galaxy stellar mass function, stellar mass-black hole mass relation, and stellar mass-size relations (see Crain et al. 2015 for details and motivation). The EAGLE reference model reproduces many observed galaxy relations that were not part of the calibration set, such as the evolution of the galaxy stellar mass function (Furlong et al. 2015b), galaxy sizes (Furlong et al. 2015a), optical colours (Trayford et al. 2015), and atomic (Bahé et al. 2016) and molecular gas content (Lagos et al. 2015), amongst others. Thus it is an excellent test-bed to compare with our observations.

We use the public database of EAGLE described in McAlpine et al. (2015). In particular, we focused our attention on the reference model of EAGLE run in a cubic volume of 100^3 Mpc³ on a side with 2×1504^3 dark matter and gas particles (particle masses are of 9.7×10^6 and 1.81×10^6 in M_\odot units, respectively, and a physical resolution of 0.7 kpc).

The full phase space information of the galaxies and the halos hosting them are provided in the simulated data. However, to facilitate comparison with the observations, we transform the given phase space information into projected space. The first step for this is to compute apparent redshift for each galaxy given its cosmological redshift (z_{snapshot}) and peculiar velocity (\mathbf{v}). We take the cartesian- z direction, with unit vector \hat{e}_z , as the direction of line-of-sight. The formula for the apparent redshift is given by,

$$z = (1 + z_{\text{snapshot}})(1 + \mathbf{v} \cdot \hat{e}_z / c) - 1, \quad (1)$$

where c denotes the speed of light.

Besides the properties of individual galaxies, we must also estimate parameters for the groups within EAGLE. To be consistent with the observational galaxy group catalogue of GAMA, we use the galaxy groups in EAGLE found using a FoF method, where a linking length of 0.2 times the average inter-particle spacing has been assumed. For more details about the group finding in the EAGLE data refer to Schaye

et al. (2015). The position of the centre of the gravitational potential well corresponds to the position of the most bound particle in the group.

2.4 Intricacies of the data: deriving galaxy and group properties

Here, we describe the derivation of the galaxy and group parameters relevant to our study in each of our data sets. The galaxy properties needed for this work are stellar mass and projected distance from the central galaxy of the group. Similarly, the group information required in our study are: the position of the group central galaxy, overall velocity dispersion of the galaxies, and virial mass and virial radius of the host halo. In some cases, those are already provided by the respective survey teams such as: central galaxy, halo virial mass, radius etc in EAGLE; group centre, stellar mass in GAMA or the GAMA-Mock. However, to ensure consistency, where possible, we re-estimate the above quantities for all the three data sets using a common method as described below:

2.4.1 Galaxy stellar mass (M_*):

We estimate the galaxy stellar mass for GAMA and GAMA-Mock using a colour-based relation

$$\log[M_*/(h^{-1}M_\odot)] = -0.4i + 0.4\mu(z) - \log(1+z) + (1.2117 - 0.5893z) + (0.7106 - 0.1467z)(g-i) - 2\log(h/0.7), \quad (2)$$

where M_* is the stellar mass expressed in the units of solar mass M_\odot , z is the galaxy redshift, g and i are the observed GAMA g and i band apparent Kron magnitudes and $\mu(z)$ is the luminosity distance modulus. Both g and i are in the observer's frame and thus, implicitly accounts for a k-correction as well as stellar population as a function of colour. The above formula is adopted from Bryant et al. (2015) and is derived following the approach of Taylor et al. (2011). In the case of EAGLE data we directly use the provided stellar mass values. Note we do this to avoid applying uncertain k-correction terms to get the data in observed rather than the native rest-frame.

2.4.2 Group occupancy (N_{FoF}):

In this work we utilise the latest version of the GAMA galaxy group catalogue (G³C v08). The FoF grouping parameters are tuned to the mock catalogues and were optimized for groups with $N_{\text{FoF}} > 4$, where N_{FoF} is the number of members grouped together by the FoF algorithm. A visual inspection of the phase space (distance-velocity plane) of GAMA groups confirms that groups with $N_{\text{FoF}} \leq 4$ are more contaminated by interlopers (Robotham et al. 2011, refer to the Fig.13 which shows the group quality as a function of N_{FoF}), while member selection for groups with $N_{\text{FoF}} > 4$ is in better agreement with the expectation of a smooth distribution of galaxies with a maximum velocity that decreases with radius. We therefore restrict our study to GAMA groups with $N_{\text{FoF}} > 4$, and impose the same limit on the GAMA-Mock and EAGLE groups as well.

2.4.3 Group centre and projected distance (R):

Robotham et al. (2011) identify the group centre in each group using three definitions of group centre: the moments derived centre of light (Cen), an iterative method rejecting the galaxy farthest away from the centre of light (recalculated at each iteration) until one galaxy is remained (the 'iterative' centre IterCen), and the brightest group galaxy (BGG). All galaxies that are not central galaxies are classified as satellite galaxies. In most cases ($\sim 90\%$) the iterative central galaxy coincides with the BGG, while the centre of light is more discrepant. Viola et al. (2015) perform a detailed analysis of the lensing signal of GAMA groups comparing the different centre definitions and confirm the results of Robotham et al. (2011), that is the BGG and the iterative centre both represent the group centre to a good degree, while the centre of light poorly represents the group centre. We consider the brightest absolute r-band magnitude galaxy in groups as a proxy for the BGG and also as the central galaxy of the group as per Robotham et al. (2011). However, we investigate the robustness of our results to different group centre definitions in Section 4.2. Once identified, we exclude the central¹ galaxies from our analysis and only keep the satellites. The group centric distance R (in units of h^{-1} Mpc) is essentially a projected comoving distance separation of the satellite galaxy to the right ascension (RA) and declination (Dec) of the group centre.

2.4.4 Group virial mass (M_{200}) and radius (R_{200}):

There are different ways to estimate the total dynamical mass of the host halo associated with galaxy groups. For example, using weak lensing (e.g. Brainerd et al. 1996; Guzik & Seljak 2002; Sheldon et al. 2004; Parker et al. 2005; Viola et al. 2015; Han et al. 2015, etc), from abundance matching (e.g. Behroozi et al. 2010; Moster et al. 2010; Behroozi et al. 2013; Hearin et al. 2013, etc), from halo occupation (e.g. Berlind & Weinberg 2002; Bullock et al. 2002; Tinker et al. 2005, etc), from conditional luminosity function based modellings (e.g. Yang et al. 2003; Cooray 2006, etc), from the velocity dispersion of galaxy groups using the virial theorem (e.g. Carlberg et al. 1997a; Schneider 2006, etc) etc. The virial mass ($M_{200}/(h^{-1}M_\odot)$) and the virial radius ($r_{200}/(h^{-1}\text{Mpc})$)² for a given redshift z are connected through the relation:

$$M_{200} = \frac{4\pi}{3} r_{200}^3 \Delta \rho_{\text{crit}}(z). \quad (3)$$

Here, we use the critical density $\rho_{\text{crit}} = 3H^2(z)/(8\pi G)$, the halo average density is $\Delta = 200$ times the ρ_{crit} and the Hubble parameter as a function of redshift $H(z) = H_0 \sqrt{\Omega_M(1+z)^3 + \Omega_\Lambda}$ assuming no curvature and a negligible radiation contribution.

To assign total halo masses to groups in our catalogues, we adopt the virial theorem based approach. But we discuss the effects of using different halo mass measurements in

¹ Note, by construction the $\sim 60\%$ of ungrouped galaxies in GAMA are simply central galaxies of a halo, where GAMA is not deep enough to observe any satellites.

² to convert spherical radius r into projected radius R and vice versa we use $r = \pi R/2$ (Schneider 2006, Equation 6.26).

our final results (Section 4). Our virial measurements adopt the conventional definition, i.e., the virial radius r_{200} is the radius in which the mean enclosed density is larger than $\Delta = 200$ times the critical density at the respective redshift $\rho_{\text{crit}}(z)$. From the virial theorem we get

$$\frac{GM_{200}}{r_{200}} = (\sqrt{\alpha}\sigma_v)^2, \quad (4)$$

where the parameter α defines the nature of the overall velocity distribution of member galaxies in group. Here, we assume $\alpha = 3$ as suggested in, e.g., [Carlberg et al. \(1997b\)](#); [Schneider \(2006\)](#) etc, which is valid for a case of isotropic velocity distribution. We estimate the group velocity dispersions (σ_v), using the technique known as the gapper-method presented in [Beers et al. \(1990\)](#), and also used in e.g. 2dFGRS Percolation Inferred Galaxy Group (2PIGG; [Eke et al. 2004](#)), SDSS ([Yang et al. 2007](#)), zCOSMOS ([Knobel et al. 2009](#)), GAMA ([Robotham et al. 2011](#)) etc. Finally, solving Equations 3 and 4 simultaneously we obtain the values for both M_{200} and R_{200} for each galaxy group. Again, the same method is used to measure virial properties of the group catalogues of all the three sets of data.

For the galaxy groups in the EAGLE catalogue, M_{200} and R_{200} are already given/known. Thus we can compare our estimate of virial properties obtained using empirical method discussed above against the supplied values. Figure 1 shows the comparison between the estimated virial properties, i.e. $M_{200}(\sigma_v, z)$ and $R_{200}(\sigma_v, z)$ against the corresponding values intrinsically known from the EAGLE simulations. The solid, dashed and dotted lines in the figure represent the loci where the ratio of intrinsic and computed virial properties are 1:1, 1:2, and 1:5 respectively. Both the M_{200} and R_{200} largely agree with each other at high masses and large radii. However, in the regions where $R_{200}(\sigma_v, z) \lesssim 0.1$ and $\log(M_{200}(\sigma_v, z)) \lesssim 11.5$ we can see significant deviation from the diagonal lines. Note, the coloured pixels show number counts in a logarithmic scale. As such, the number of discrepant groups at low M_{200} or R_{200} is small. Nevertheless, there is a clear disagreement at low mass or radius. The disagreement is potentially due to a number of reasons. For example, the underlying assumption in our estimates of R_{200} and M_{200} from Equations 4 and 3 is that the groups are virialised and are characterised by an isotropic distribution of velocities ($\alpha = 3$), which may not necessarily be the case ([Diaferio et al. 1993](#)). In case of anisotropy, α could be off by up to a factor of two ([Mahdavi et al. 1999](#)) resulting in systematic errors in our estimates. However, in our subsequent analysis we only use halos with $\log(M_{200}) \geq 12$, where the agreement between the estimated and intrinsic virial properties is reasonably good. Note, ideally the halos with intrinsic halo mass $\log[M_{200}/(h^{-1}M_\odot)] \lesssim 13$ and empirically measured halo mass $\log(M_{200}(\sigma_v, z)) \lesssim 12$ would have been included in our sample if the calibration given by Equation 4 was perfect. Since each halo is expected to be individually stellar mass limited at a given redshift, the effect of the missed halos due to poor halo-mass calibration will only be in the overall statistics in a given halo mass bin.

As a reference, in Figure 2 we show the joint distributions of the stellar mass (M_*) of the satellite galaxies in groups as a function of halo mass (M_{200}) of the corresponding groups for all the three data sets (GAMA, GAMA-Mock

and EAGLE). Note that the figure shows all the galaxies in groups, thus they may not be necessarily complete in stellar mass. The figure is only presented to provide additional insight into the data, and also to guide the appropriate halo mass selection ranges that we use in this paper.

2.4.5 Volume limited samples

The shortcoming of a magnitude limited survey like GAMA is that it observes a small (large) volume for the less (more) luminous galaxies. In other words, the mass completeness limit of the survey varies as a function of redshift. Figure 3 shows the stellar mass-redshift relation for all data sets highlighting the varying mass incompleteness as a function of redshift. To tackle the bias introduced by this incompleteness (Malmquist bias), we adopt a conservative but robust approach of sub-selecting a volume complete sample. For this we have to first estimate a reasonable lower limit on stellar mass as a function of redshift. This is determined using the running 90th percentile of the stellar mass distribution of the galaxies in groups at all redshifts. For the discussion on the choice of percentile and its effect on our final results refer to the Appendix A. In summary the precise choice of stellar mass limit has no discernible impact on our primary results concerning stellar mass segregation.

We show the stellar mass completeness boundary with the white line in the top panel of Figure 3. The coloured pixels in the figure show the joint distributions of the galaxy stellar mass and redshift, where the colour scale depicts the logarithmic number count of galaxies in the underlying pixel. The redshift ranges we use are $0 < z \leq 0.14$, $0.14 < z \leq 0.22$ and $0.22 < z \leq 0.32$, and are chosen such that their mid-values are roughly equal to the redshift corresponding to the available snapshots of the EAGLE simulation. In these redshift ranges for the GAMA data, we determine the minimum complete log stellar mass values to be of 9.1, 9.7 and 10.0 respectively. The horizontal red lines in the figure are the demarcation of the lower-bound in the stellar mass at each redshift range. We will also present results for a single $z \leq 0.32$ range, where we assume a conservative mass completeness lower-limit of $\log(M_*/M_\odot) = 10.0$.

The synthetic GAMA-Mock and EAGLE data are complete down to the resolution limit of the simulation. However, for an effective comparison with the observed data, we impose a magnitude limit of $r_{\text{mag}} < 19.8$ mag (identical to the observed GAMA data). To calculate stellar mass limits for the simulated data (GAMA-Mock and EAGLE) we repeat the same exercise as in the GAMA data. In the redshift ranges given above even for the simulated data, we find the lower limit in stellar mass to be similar to the GAMA data. However, to make the final analysis comparable we impose exactly the same minimum limit on the stellar mass of the GAMA data to all the three sets of data. The middle and bottom panels of Figure 3 shows the the stellar mass-redshift joint distributions for our GAMA-Mock and EAGLE samples. Again, the horizontal red lines show the demarcation of the lower limit in the stellar mass at each redshift range whereas the vertical red lines divide the redshift range in which latter we study mass segregation. Note, the discreteness in redshift seen in the bottom panel, which shows the EAGLE data, is due to the fact that the hydrodynamical

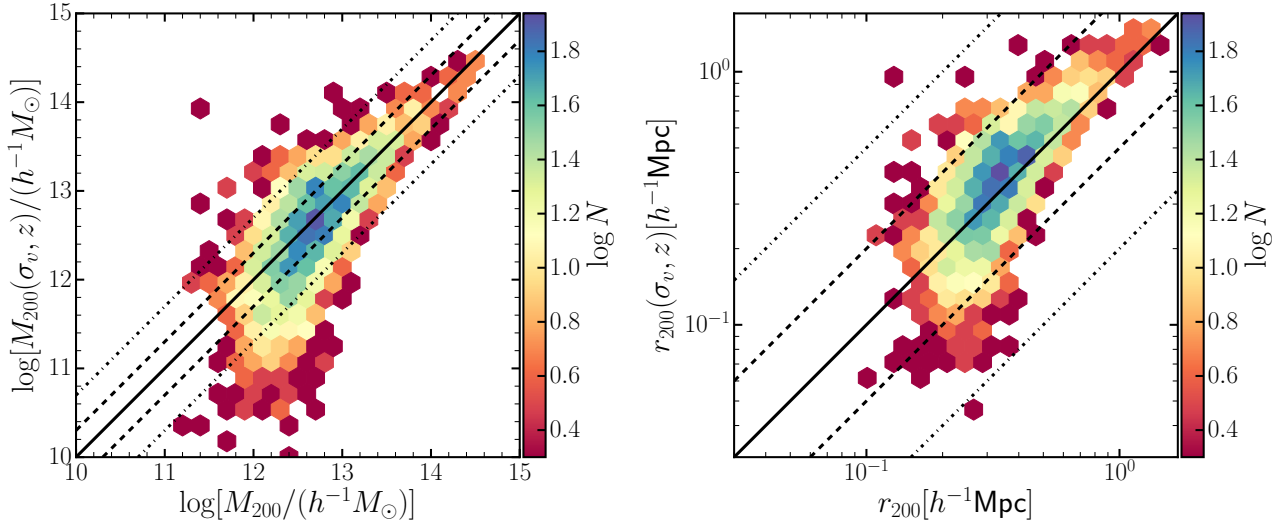


Figure 1. Comparison of intrinsic (along horizontal axis) and estimated (along vertical axis) virial properties of the EAGLE galaxy groups. The panel on the left shows comparison of the halo masses $\log(M_{200})$ whereas panel on the right compares the halo virial radius r_{200} . The solid, dashed and dotted lines are 1:1, 1:2, and 1:5 demarcation lines respectively. The colour of each pixel represents log number count of galaxies as labelled in the colour bar alongside.

simulation provides snapshots of the simulated universe at the discrete redshifts.

3 RESULTS

The main aim of this study is to investigate mass segregation of satellite galaxies in galaxy groups, and its dependence on halo mass. An additional by-product of this is the investigation of the redshift evolution of the spatial distribution of galaxy mass in groups. In general, there are very few high multiplicity groups within the observational limits of the GAMA ($r_{\text{petro}} < 19.8$), and likewise in the GAMA-Mock and EAGLE data once the magnitude limit is applied, which means we are unable to study stellar mass distributions on a group by group basis. To enhance the signal we stack groups and study their average properties instead, as done in previous similar studies (e.g. Wetzel et al. 2012; Zipparo et al. 2013; Roberts et al. 2015, etc). For stacking, we scale the group-centric projected distance R of the galaxy by the virial radius R_{200} of the group, which should make the group size scale free. We then investigate the stacked properties of group galaxies in halo mass $\log[M_{200}/(h^{-1}M_{\odot})] \in [12.0, 12.5], (12.5, 13.0], (13.0, 13.5]$ and $(13.5, 14.5]$ ranges.

3.1 Analysis of mass segregation in galaxy groups

First, we study how the stellar mass, $\log(M_{\star})$, of the satellite galaxies in groups varies with the scaled group-centric radii R/R_{200} in each of our halo mass $\log[M_{200}/(h^{-1}M_{\odot})]$ ranges. In the left column of Figure 4, we show the mean (by solid lines) and median (by faint uneven dashed lines) values of the $\log(M_{\star})$ of satellite galaxies in different R/R_{200} and M_{200} ranges. The top (panels a and d), middle (panels b and e) and bottom (panels c and f) rows demonstrate the distributions of the GAMA, GAMA-Mock and EAGLE data respectively. The

$\log[M_{200}/(h^{-1}M_{\odot})] \in [12.0, 12.5], (12.5, 13.0], (13.0, 13.5]$ and $(13.5, 14.5]$ are shown in black, red, blue and green colours respectively. Furthermore, the faint dashed lines below and above the solid dashed lines show the 16th and 84th percentiles of the distribution. The redshift range of the data in this case is $z \leq 0.32$ and limited to $\log(M_{\star}) \geq 10.0$ to guarantee stellar mass completeness (as described in Section 2.4.5). Moreover, we divide the data in five R/R_{200} ranges: $(0.0, 0.32], (0.32, 0.64], (0.64, 0.96], (0.96, 1.28]$ and $(1.28, 2.0)$. Error bars shown in the data points in all the figures are the standard error of means for samples in the given halo mass and scaled radius ranges. For all of our mass segregation trends we fit a straight line with the uncertainties taken into account as described in Hogg et al. (2010); Robotham & Obreschkow (2015). The solid, dashed or dotted lines shown in all the figures throughout the paper show the resultant best fit models.

There are few common trends that emerge from all three sets of data presented in panels (a), (b) and (c) of Figure 4. First, both the mean (solid lines) and median values (faint uneven dashed lines) of $\log(M_{\star})$ show consistently similar trends. Thus, for clarity, and also for a sake of convenience in comparing with the literatures, we subsequently highlight the mean $\langle \log[M_{200}/(h^{-1}M_{\odot})] \rangle$ and show other central tendencies such as medians and percentiles with fainter lines. Secondly, the mean trend lines (solid lines) show negligible gradients with the scaled-radius out to twice the group virial radii. As such we fail to detect mass segregation ubiquitously for all the three data sets in the redshift range $z \leq 0.32$. Moreover, the absence of mass segregation trends seems independent of the halo mass range. The slopes of our best fit mass segregation trends for all three data sets are $\lesssim 0.04$ dex.

We note in all three panels (a), (b) and (c) of Figure 4 that the 16th percentile of the $\log(M_{\star})$ distributions (shown by faint dashed lines sitting below the solid lines), irrespective of the halo mass range, are clumped together

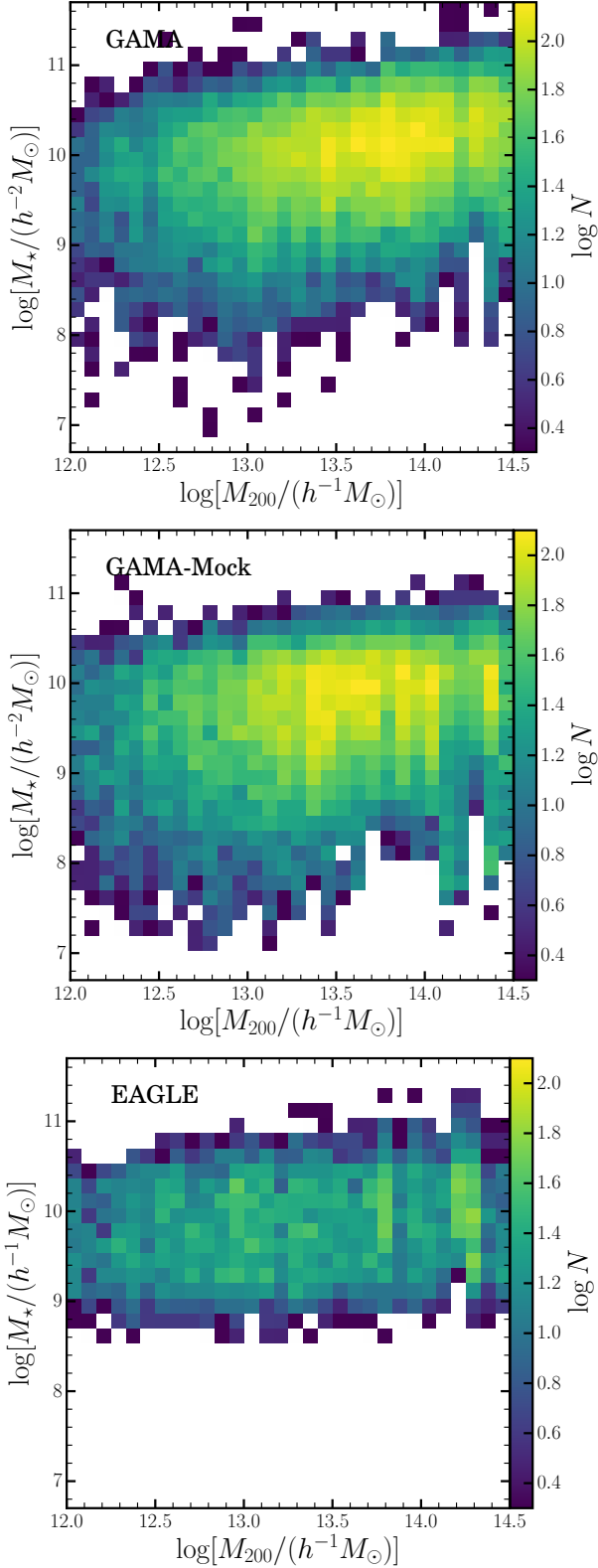


Figure 2. Stellar mass (M_*) of the satellites versus the host halo mass (M_{200}) as labelled in each panel from top to bottom is GAMA, GAMA-Mock and EAGLE data. The colour of each pixel represents log number count of galaxies as labelled in the colour bar alongside. Note, this shows the entire sample for all the three data sets and is not just limited to the stellar mass complete sample.

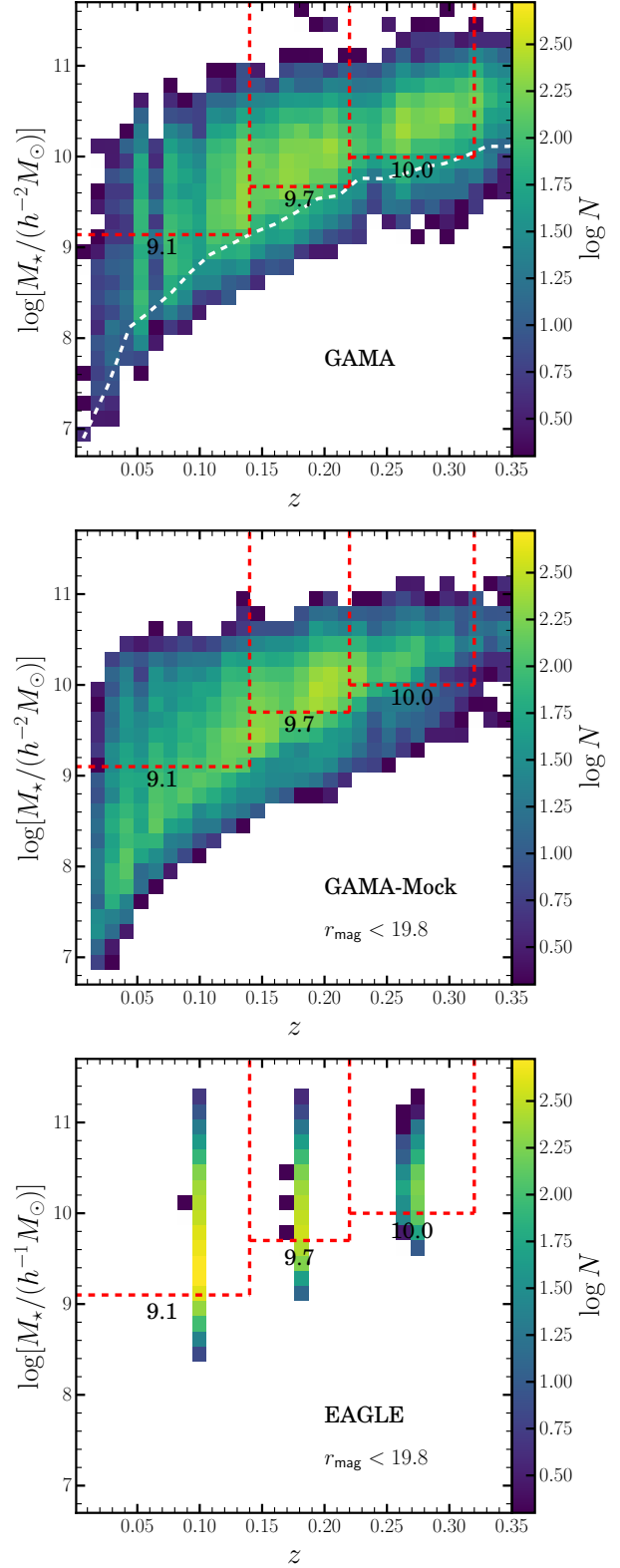


Figure 3. Determination of the stellar mass completeness as a function of redshift. The panel at the top shows GAMA data, the middle-panel shows the GAMA-Mock and the bottom one shows EAGLE data. All panels show stellar mass-redshift joint distributions colour coded by counts in the log scale. Dashed red lines show stellar mass complete sample in different redshift windows. The white dashed line on the top-left panel is the running 90th percentile of the distribution.

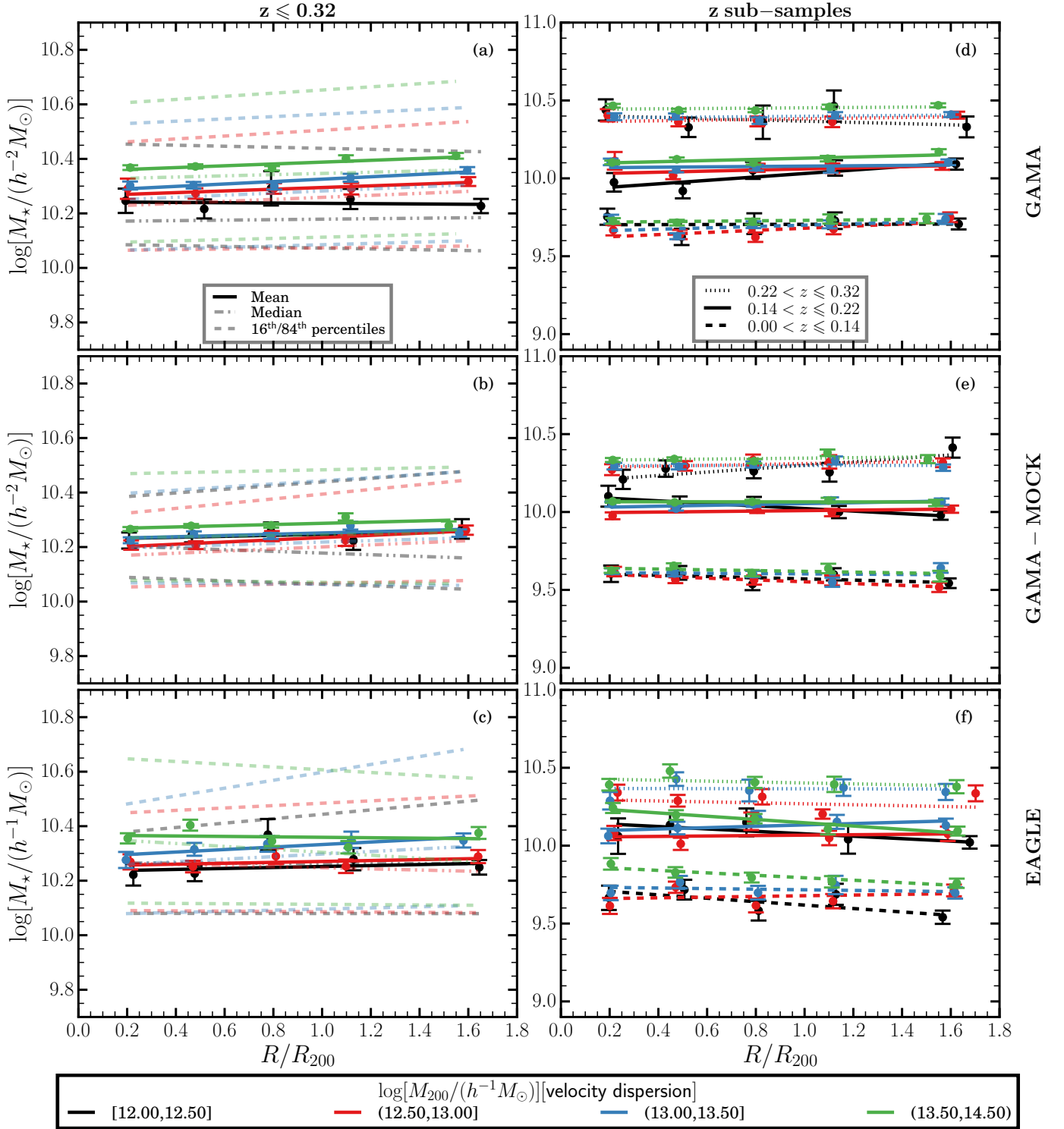


Figure 4. Stellar mass distributions of satellite galaxies in the galaxy group catalogues taken from GAMA (top row), GAMA-Mock (middle row) and EAGLE (bottom row). In all panels, different colours represent different halo mass range. The left column shows the radial runs of the central-tendency of $\log(M_*)$ of the galaxies in galaxy groups of different halo mass ranges for $z \in (0.00, 0.32]$ with $\log(M_*) \geq 10.0$. Means of the $\log(M_*)$ are shown with solid lines and medians are shown with faint dashed-dotted lines whereas the faint dashed lines above(below) the solid lines are the 84th(16th) percentile of the $\log(M_*)$ in a given data range. The column in the right side shows expectations of $\log(M_*)$ in different redshift sub-samples as a function of halo mass. Here, the dashed, solid and dotted lines represent means of the $\log(M_*)$ in $z \in (0.00, 0.14]$ with $\log(M_*) \geq 9.1$, $z \in (0.14, 0.22]$ with $\log(M_*) \geq 9.7$ and $z \in (0.22, 0.32]$ with $\log(M_*) \geq 10.0$ respectively.

near the limiting mass of our volume limited sample. This is due to a hard lower-limit set on the stellar mass as a function of redshift (Figure 3). On the other hand, the 84th percentile of the $\log(M_*)$ distributions (faint dashed lines sitting above the solid lines in the figure) show higher normalisation with increasing halo mass. For example, for the GAMA data (panel a) the green lines representing the highest $\log[M_{200}/(h^{-1}M_\odot)]$ group are above the blue lines, followed by red with the black line representing the smallest $\log[M_{200}/(h^{-1}M_\odot)]$ groups at the bottom. It is due to a complex combination of occupation physics that we observe higher mass halos hosting, on average, more massive galaxies. This is a well understood effect (e.g. Conroy et al. 2006; Behroozi et al. 2010; Moster et al. 2010; Guo et al. 2010; Behroozi et al. 2013, etc) and is also observed in the earlier Figure 2, where the $\log(M_*)$ versus $\log[M_{200}/(h^{-1}M_\odot)]$ joint distributions have positive gradients.

3.2 Lack of evidence of redshift evolution in satellite stellar mass distribution

Here, we investigate the redshift evolution of the distribution of the stellar masses in galaxy groups. For this analysis, we separate our data, in particular, GAMA and GAMA-Mock, into the three redshift ranges $z \in (0, 0.14]$, $(0.14, 0.22]$ and $(0.22, 0.32]$. As discussed in Section 2.4.5, these ranges are chosen such that their mid-values roughly equal to the redshift corresponding to the available snapshots of the EAGLE simulation. Also, as discussed earlier (again in Section 2.4.5), to avoid the Malmquist bias the above samples are then stellar mass limited to $\log(M_*) \leq 9.1$, ≤ 9.7 and ≤ 10.0 respectively.

All panels (d), (e) and (f) in the right column of Figure 4 show the redshift evolution of the stellar mass distribution in the groups out to twice the group virial radius. The dashed, solid and dotted lines here show the mean $\log(M_*)$ in increasing order of redshift. As mentioned earlier, the mean and median values of $\log(M_*)$ are consistent with each other and hence, here we only show mean values for clarity. The different colours denote different halo mass ranges as labelled at the bottom of the figure. Here we again we bin the data in radial ranges, $R/R_{200} \in (0.00, 0.32]$, $(0.32, 0.64]$, $(0.64, 0.96]$, $(0.96, 1.28]$ and $(1.28, 2.0]$.

In panels (d), (e) and (f) of Figure 4, a clear normalisation shift of $\log(M_*)$ as a function of redshift can be seen. The shift is an artefact introduced due to the different lower limits on $\log(M_*)$ imposed on the data for different redshift brackets while creating a stellar mass-limited sample (red-dashed lines in Figure 3). This systematically offsets the mean values, i.e. at high redshifts we do not detect the lower mass galaxies and hence the mean stellar mass is higher. There are a few ways to rectify this effect. For example, instead of $\log(M_*)$ one could use $\log(M_*)$ scaled by central satellite galaxy mass or the $\log(M_*)$ renormalised by the median $\log(M_*)$ values of the distribution of galaxies in each red boxes from the corresponding panels in Figure 3. Moreover, one can also fit a stellar mass function (e.g., Baldry et al. 2012; Moffett et al. 2016; Weigel et al. 2016, etc) separately for all redshift ranges and then scale the $\log(M_*)$ by the obtained break mass. However, since the main objective of our work is to investigate the gradient of the distribu-

tions and not their normalization, we leave the distributions unscaled and note this effect.

In Figure 4(f) for EAGLE data with $\log(M_{200}) \in (12.00, 12.5]$ and $z \in (0.00, 0.14]$, shown with black dashed line, we see a mild segregation trend with a gradient of -0.11 ± 0.06 dex. Also, we note that the GAMA-Mock data (Figure 4e) with $z \in (0.22, 0.32]$ at $R/R_{200} < 0.5$ and $\log[M_{200}/(h^{-1}M_\odot)] \in [12.00, 12.50]$ show a strange increasing trend with slope 0.11 ± 0.05 dex. This is in a contrast to what we observe in the corresponding GAMA data in panel (d) and for EAGLE data in panel (f). This contradicting behaviour is due to the difference in $\log(M_*)$ and $\log[M_{200}/(h^{-1}M_\odot)]$ joint distributions at $z \in (0.22, 0.32]$ in the top and mid panels in Figure 3. Overall, comparing panels (d), (e) and (f) of Figure 4 we conclude that in overall there is negligible mass segregation in the groups with absolute gradient $\lesssim 0.08$ and consistent to zero when uncertainties in the slope is considered. Interestingly, the satellite stellar masses as a function of scaled group radii for all the three data sets do not show any redshift evolution either.

3.3 Mass segregation in EAGLE data out to $r < 22$ mag?

The EAGLE data can give us more insights into the stellar mass distribution of satellite galaxies in groups beyond what current observable data can offer. In particular, it allows us to probe galaxies, and hence groups, at fainter magnitude, and to observe stellar mass distributions in 3D space with theoretically intrinsic values for key quantities such as $\log(M_*)$ and $\log[M_{200}/(h^{-1}M_\odot)]$ instead of the estimated values based on simple observed scaling relations.

The stellar mass resolution limit of the EAGLE simulation is $\log(M_*) > 8.2$. This means we can probe to a fainter magnitude limit of $r_{\text{mag}} < 22$ allowing us to make predictions that can be tested with group catalogues generated from the future redshift surveys such as WAVES (Driver et al. 2015). The apparent magnitude limit to $r < 22$ mag means we can now study satellite mass distribution out to a redshift $z \leq 0.75$. Results shown in the top panels (a) and (b) of Figure 5 are obtained repeating the same analysis as in the bottom panels (c) and (d) respectively of Figure 4, but with the fainter magnitude limited sample of $r < 22$ mag.

In addition, EAGLE also provides the full 3D distributions of the galaxies in groups. In Figure 5 (c) and (d), we show the mass segregation in EAGLE groups for $r_{\text{mag}} < 22$ using the intrinsic values for the $\log(M_*)$, $\log[M_{200}/(h^{-1}M_\odot)]$, and spherical radius (r) instead of the projected radius. We undertake this exercise with an ideal data set to highlight that the lack of mass segregation is possibly physical and not simply the manifestation of projected data and the approximate galaxy/group properties we use in reality. Panels (a) and (c) of the figure show spatial distributions of the satellite mass $\log(M_*) \geq 10.1$ in the given ranges of host halo mass to a redshift range of $z \leq 0.75$. In the figure, we once again show the mean, median and the percentiles (16th at the bottom, 84th at the top) of the $\log(M_*)$ by solid, faint dashed-dotted and faint dashed lines respectively. Similarly, panels (b) and (d) show the spatial distributions of the satellite mass $\log(M_*)$ in the given ranges of host halo mass in 5 different redshift ranges.

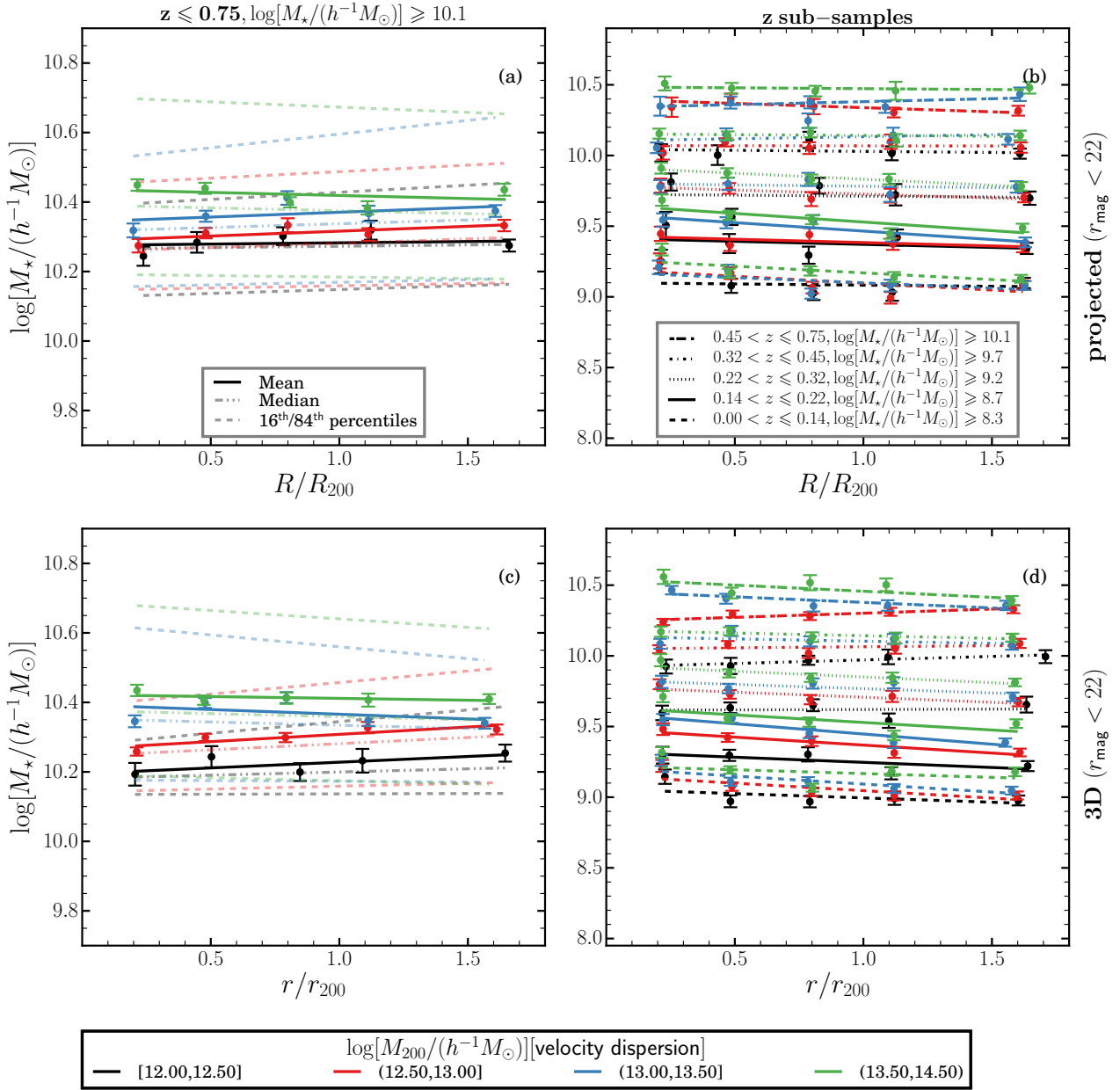


Figure 5. Radial distribution of the stellar mass of the satellite galaxies in EAGLE galaxy groups out to a fainter magnitude limit of $r_{\text{mag}} < 22$. Top panels show distributions in projected space, i.e., in observational space with inferred values for the masses. Bottom panels show the distributions using the full 3D information of the galaxies in groups and also, using the intrinsic values for stellar and halo masses. The meanings of the different line types in the above figure are identical to Figure 4.

For clarity we do not show the percentiles in the right side panels. In all panels, different colours represent different host halo mass ranges.

Overall, in panels (a) and (b) we again observe negligible mass segregation with absolute gradient of $\lesssim 0.03$ dex and $\lesssim 0.09$ dex respectively. Similarly, in panel (c) and (d), which uses the ideal data, we still do not observe any radial gradients in stellar mass runs. All these results hold irrespective of the host halo mass. However, in panels (b) and (d) for the cases $z \leq 0.22$ there is seemingly some mild mass segregation with slopes ranging between 0.06–0.1 dex albeit with large uncertainties of typically 40%. Given that at $z \leq 0.22$

we are closer to the mass resolution of the EAGLE simulation (Schaye et al. 2015) it is difficult to be certain that this result is robust to simulation resolution limits. However, in all other cases, i.e., $0.75 \geq z > 0.22$ the stellar mass distribution is almost flat once again demonstrating the lack of mass segregation.

As evidenced in Figure 1, there are uncertainties on the estimated virial radius R_{200} . Hence, it is possible that for a large enough uncertainty on R_{200} , and therefore also in scaled radius R/R_{200} , any real underlying radial trend could be erased. Due to a lack of intrinsic/true measurements of R/R_{200} it is difficult to simulate this effect on GAMA and

GAMA-Mock. The EAGLE data would be useful here as both the intrinsic and projected/noisy R/R_{200} information are available. However, in the case of the EAGLE data we have already seen in Figure 5 that there is no segregation trend even when the intrinsic properties are considered. Therefore, for this simulation we generate a synthetic stellar mass for EAGLE galaxies sampled from a straight line of gradient $= -0.3$ dex, roughly of the same magnitude as seen in some literature, and also, introduce a normally distributed scatter of 0.35 dex around the line, which is a function of intrinsic R/R_{200} . We then fit a straight line to the synthetic stellar mass as a function of noisy/observed R/R_{200} with inherent error distributions as shown in Figure 1. Given the uncertainties in R/R_{200} we were still able to recover the slope with $\lesssim 10\%$ uncertainty. The uncertainty is close to 10% for the lowest halo mass range whereas slightly smaller for the highest halo mass range. The above exercise suggests that the associated uncertainties in the derived virial properties do not erase the signal unless the gradient is as tiny as 0.03 dex.

4 DISCUSSION

4.1 Robustness of the absence of mass segregation to different halo mass estimates

As discussed earlier, the total dynamical mass of a group can be estimated in numerous ways, such as from its velocity dispersion using the virial theorem (e.g. Carlberg et al. 1997b; Schneider 2006, also Equation 3, etc), from weak gravitational lensing (e.g. Brainerd et al. 1996; Parker et al. 2005; Viola et al. 2015, etc), from its luminosity assuming some light-to-mass ratio or from abundance matching (e.g. Behroozi et al. 2010; Moster et al. 2010; Behroozi et al. 2013; Hearin et al. 2013, etc) etc. An independent measurement of the halo mass using different methods for all three data sets is a massive undertaking and well beyond the scope of this work. However, the GAMA group catalogue readily provides some alternative measurements of halo mass. Thus, here we confine our study to only the GAMA group catalogue.

For reference we remind the reader that the mass segregation trends in GAMA groups with virial theorem (velocity dispersion) based halo masses are presented in Figure 4(a). Now, in Figure 6 we show the same as Figure 4 but with halo mass $\log[M_{200}/(h^{-1}M_{\odot})]$ measured from three additional methods, (i) abundance matching using halo occupation distribution (Tinker et al. 2012), (ii) group total luminosity (Robotham et al. 2011) and (iii) the weak lensing calibrated relation (Viola et al. 2015). Results from these different halo mass estimates are shown in panels (a), (b) and (c) of Figure 6 respectively. Note, the R_{200} used here are also recomputed for the different definition of $\log[M_{200}/(h^{-1}M_{\odot})]$ using Equation 3. In panels (b) and (c), due to sparse data we are only able to probe above $\log[M_{200}/(h^{-1}M_{\odot})] \geq 12.5$, whereas due to an increase in number counts in $\log[M_{200}/(h^{-1}M_{\odot})] \in (13.00, 14.50]$ we split it into further two bins $(13.00, 13.50]$ and $(13.50, 14.50]$. For all three cases typical values of the slopes of the mass segregation is 0.02 ± 0.02 dex meaning there is still no segregation in GAMA data highlighting that the lack of observed mass segregation is not due to our choice of

halo mass estimator. The exception to this is the case of $\log[M_{200}/(h^{-1}M_{\odot})] \in [12.5, 13.0]$ range (Figure 6b) and $\log[M_{200}/(h^{-1}M_{\odot})] \in [13.5, 14.5]$ (Figure 6a) where we do see some mild segregation trend with slope of $\sim |0.04|$ dex, which we did not detect using the dynamically implied halo masses. It could potentially be due to sample size fluctuation as a result of scatter between halo mass estimates obtained using different methods. Overall, the trends for larger halo masses for all four halo mass measurements are broadly consistent. This comparative study gives us confidence that the lack of mass segregation, at least in the case of GAMA observational data, is robust to the halo masses used.

4.2 Robustness of the absence of mass segregation to different group centre definitions

As discussed earlier, a centre of any galaxy group can be pinned to be at its luminosity weighted centre or at the location of its brightest group galaxy (BGG). The GAMA group catalogue provides both the measurements of group centre. Here, we use them to test the robustness of the absence of mass segregation to the different definitions for the group centre. Figure 4(a) already shows the mass segregation in GAMA groups assuming BGGs as the group centres. Therefore in Figure 7 we repeat the analysis for GAMA groups assuming the luminosity weighted centre (labelled as Cen in the catalogue). Except for the lowest halo mass bin where scatter in the data is large, slopes of the trends for all the other halo mass ranges are consistent with zero. Comparing Figures 4(a) and 7 it can be concluded that the effect of the above mentioned choices of the group centre is on average negligible on the mass segregation trends in GAMA data.

4.3 Mass segregation in SDSS?

Here we compare our results to mass segregation studies reported in the literature that use SDSS group catalogues. In a study using a V_{\max} weighted sample based on the SDSS DR4 galaxy group catalogue of Y07, van den Bosch et al. (2008) find a significant mass segregation gradient of ~ 0.5 dex over an extent of one virial radius³. Additionally, they find that the mass segregation occurs at all halo mass ranges. Interestingly, more recent work in Roberts et al. (2015), again based on Y07 (but using SDSS DR7), presents a slightly different picture than the previous work. For example, for their case of $\log(M_{\star}) > 9.0 + V_{\max}$, which is equivalent to van den Bosch et al. (2008) studies, we see that the magnitude of spatial mass segregation is $\lesssim 0.2$ dex for the low halo mass ($\log[M_{\text{halo}}/(h^{-1}M_{\odot})] < 13$) case, and it is almost negligible ($\lesssim 0.05$ dex) for larger halos. In contrast to above works, using galaxy group catalogue created from SDSS DR7 but with modified implementation of the Y07 group-finder, Wetzel et al. (2012) fail to detect evidence for satellite mass segregation at any halo mass range. This result is in overall

³ It should be noted that the range of the scaled radius varies depending on the choice of over-density constant Δ . For example, the distance where the mean matter density of the group is $\Delta = 200$ times the mean background matter density will always be smaller than when $\Delta = 180$ is assumed. It means for the same range in R , R/R_{180} spans to smaller range compare to R/R_{200} .

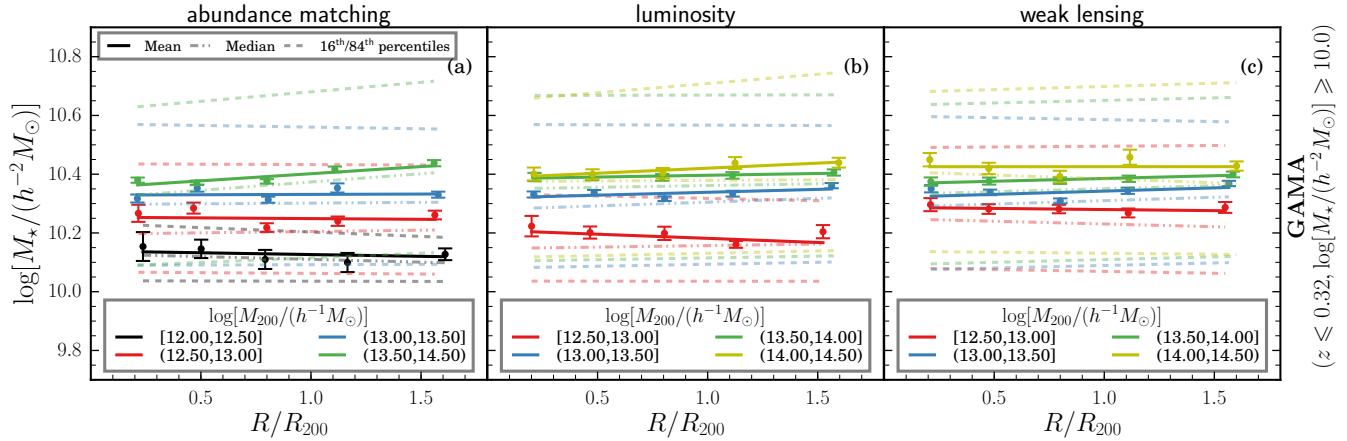


Figure 6. Stellar mass distribution of the satellite galaxies in GAMA galaxy groups in different halo mass ranges for three halo mass definitions (a) abundance matching, (b) luminosity based and (c) weak lensing. All labellings are identical to Figure 4(a), but note largest halo mass bin further split into two bins $[13.50, 14.00]$ and $[14.00, 14.50]$.

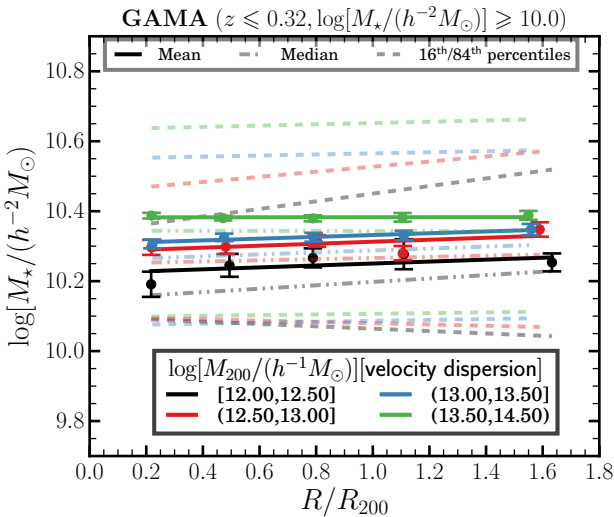


Figure 7. Stellar mass distribution of the satellite galaxies in GAMA galaxy groups with luminosity weighted centre. All labellings are identical to Figure 4(a).

agreement to our findings of absence of mass segregation in GAMA, GAMA-Mock and EAGLE galaxy groups.

There could be various potential reasons resulting in the contrasting mass segregation trends. For example, differences in arbitrary stellar mass completeness limit in previous studies, the subtleties of group-finding algorithms, different prescriptions for stellar/halo masses being used, different definitions for the group centres or, potentially the combination of all the above possibilities. For example, the mass segregation trends with the conservative stellar mass limited (e.g., $\log(M_*) > 10.5$) case compared to the volume-weighted $\log(M_*) > 9.0 + V_{\max}$ case in Figure 1 (note different range of y-axis in two panels) of Roberts et al. (2015) are much steeper than the latter case.

Similarly, Wetzel et al. (2012) and Roberts et al. (2015), who use the same input data, i.e., SDSS DR7, still find contradicting mass segregation trends. The main difference be-

tween the two works is in their implementations of the Y07 group finder. While the later work uses the original group catalogue, the earlier work uses a modified version of Y07. This means the subtle difference in the implementation of the group finding algorithms could be a factor.

In the following, we further investigate the source of contradicting results existing in the literature. For this, first and foremost we adopt an independent group catalogue of SDSS data by Saulder et al. (2015), constructed using the group finding algorithm similar to Robotham et al. (2011, the GAMA group catalogue). Both studies use the friend-of-friends algorithm with similar values for the linking lengths ($b_{\perp} \simeq 0.06$ and $b_{\parallel} \approx 1.0$), which are the distances that define which objects should be linked into common halos/groups. These linking lengths are tuned to reproduce the properties of mock groups. Importantly, the linking lengths used in both the above works are also the values recommended from the recent investigation on the performance of friends-of-friends algorithm among various existing group catalogues by Duarte & Mamon (2014). Secondly, to be consistent with our earlier observations with GAMA, GAMA-Mock and EAGLE, we re-estimate physical properties such as galaxy and group masses, group radius etc for the Saulder et al. (2015) group catalogue with methods described in the Section 2.4.

In Figure 8(c) we present our results for SDSS data using the Saulder et al. (2015) group catalogue. Here, to facilitate comparison with previous works with SDSS (e.g. Roberts et al. 2015, etc), we only investigate stellar mass limited sample of $\log[M_*/(h^{-1}M_{\odot})] \geq 10.2$. Also note that, like in the above subsections here also we scale group radii with corresponding R_{200} . Since we are mainly interested in the gradient of the radial distribution of the satellite stellar masses the effect of the choice of $\Delta = 180$ versus 200 is minimal in the direct comparison between results in Figures 4(a), (b), (c) and 8, and e.g. van den Bosch et al. (2008). In Figure 8(c) we demonstrate that the recent SDSS group catalogue of Saulder et al. (2015) also does not show any mass segregation, where the maximum value of the slope of trend lines for all the halo mass ranges is 0.01 ± 0.01 . This is in an agreement with our findings from GAMA, GAMA-

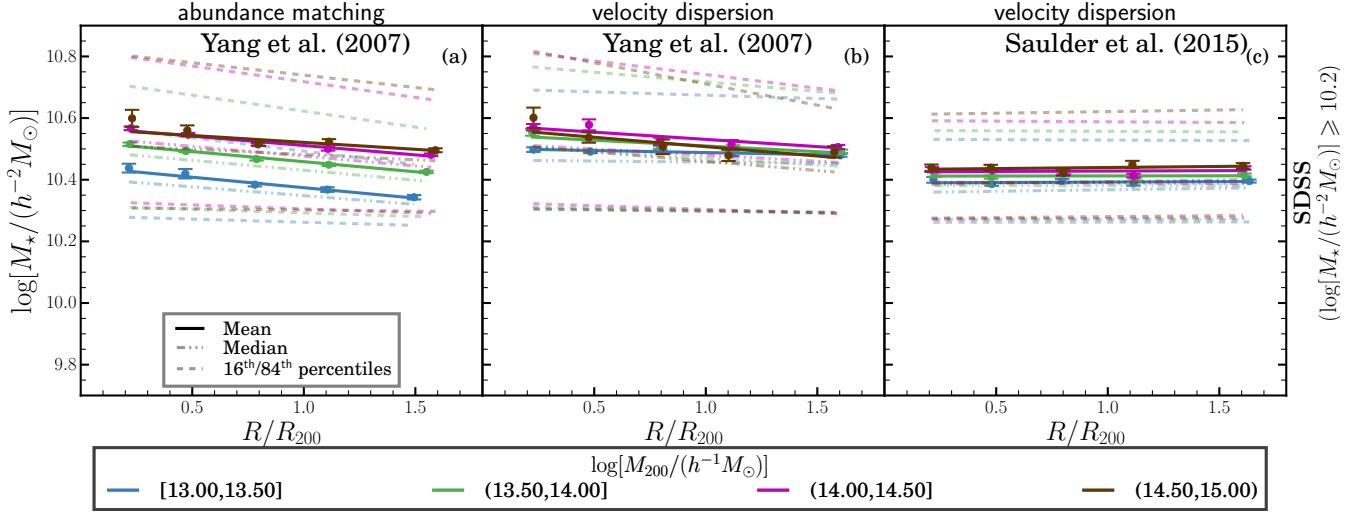


Figure 8. Spatial mass distribution in SDSS galaxy groups as a function of host halo mass. Panel (a) and (b) show results with SDSS group catalogue of Yang et al. (2007) using abundance matched and velocity dispersion based halo masses respectively. Panel (c) shows results with SDSS group catalogue of Saulder et al. (2015) using velocity dispersion based halo masses. The samples are stellar mass limited to $\log[M_*/(h^{-1}M_\odot)] \geq 10.2$. Mean values are shown with bold solid lines whereas faint lines represent percentiles as in Figure 4(a). Different colours show different halo mass ranges as depicted in the box at the bottom of the figure.

Mock and EAGLE data and also, from the studies of SDSS data by Wetzel et al. (2012) whereas in contradiction with the other studies of SDSS data by van den Bosch et al. (2008) and Roberts et al. (2015).

The differences in the mass segregation trends observed in SDSS data by Wetzel et al. (2012); Saulder et al. (2015) and by van den Bosch et al. (2008); Roberts et al. (2015) could perhaps be due to the inaccuracies associated with the group finding in the very first place. To investigate this, here, we directly adopt the group catalogue of Yang et al. (2007, Y07) for SDSS data. In Figure 8(a) we demonstrate that we recover the mass segregation trend in the Y07 group catalogue. The magnitude of mass segregation in Y07 here ranges from -0.08 ± 0.01 dex for $\log[M_{\text{halo}}/(h^{-1}M_\odot)] \in [13.0, 13.5]$ to -0.05 ± 0.01 dex for $\log[M_{\text{halo}}/(h^{-1}M_\odot)] \in (14.5, 15.0)$ i.e. segregation becomes shallower with increase in the halo masses, which are roughly consistent with earlier work by Roberts et al. (2015). To produce this result, we take the galaxy and group properties from the published group catalogue of Y07. Note, the halo masses in the Y07 catalogue are based on two measurements: the total luminosity or total stellar mass of the all group members brighter than $M_r < -19.5$. We find that using either of these two estimates for halo mass makes negligible difference in observed mass segregation. In Figure 8(b) we repeat the same analysis with the group catalogue of Y07 but using implied dynamical halo mass measured from velocity dispersion as described in Section 2.4.4, and consistent with the cases of GAMA, GAMA-Mock, EAGLE and Saulder et al. (2015) SDSS group catalogue. As a final check, for both the left and mid panels of Figure 8, we compute $\log[M_*/(h^{-1}M_\odot)]$ using the relations in Y07, which is a function of g and r band magnitudes instead of one given in Equation 2. We find that the differences of these two colour based calibrations for galaxies stellar mass has negligible influence in our result. Comparing panels (a) and (b) of the figure, we note that

the segregation is already reduced when switched to velocity dispersion based mass estimate. In particular for a case of $\log[M_{\text{halo}}/(h^{-1}M_\odot)] < 13.5$ in middle panel the segregation is almost negligible ($\lesssim 0.03$ dex from $\lesssim 0.07$ dex). This result is consistent with our findings from GAMA, GAMA-Mock and EAGLE, strictly speaking to the cases of $z \lesssim 0.14$ given the shallower redshift range of SDSS data.

If we compare Figure 8(b) with Figure 8(c) we can see that there are still some segregation trends visible in the larger $\log[M_{\text{halo}}/(h^{-1}M_\odot)] > 13.5$ cases. This could possibly be due to subtleties of group finding scheme, linking lengths, or their complex combination. Moreover, Y07 use an imprecise scheme to estimate the dependence of luminosity incompleteness on redshift in their flux-limited sample as discussed in Duarte & Mamon (2015) and is also apparent in Figure 4 of Y07. These errors in the luminosity incompleteness propagate to the inferred group masses. Thus, the dramatic decrease in the segregation trend between Figure 8(a) (equivalent to Figure 1 in van den Bosch et al. 2008) and Figure 8(b) appears to be due to the luminosity based halo mass measurements provided in Y07.

We note that van den Bosch et al. (2008); Roberts et al. (2015) consider the luminosity weighted centre as a group centre whereas Wetzel et al. (2012), Figure 8(c) using Saulder et al. (2015) and all of our analysis in the previous sections assume BGG as a group centre. Similarly, the fact that in Figure 8 (a) and (b) we are using BGG centres and still being able to recover the segregation trend in van den Bosch et al. (2008); Roberts et al. (2015) suggest that the effect of the above definitions of group centres is negligible. This is also in agreement with our conclusion for GAMA data presented in Section 4.2.

In summary, the segregation trends seen in the Y07 group catalogue of SDSS data shown in Figure 8(a) and also observed in earlier studies (Roberts et al. 2015; van den Bosch et al. 2008) are in contrast to our findings with

GAMA, GAMA-Mock and EAGLE group catalogues, as well as to the findings of [Wetzel et al. \(2012\)](#) and our Figure 8(c) with the [Saulder et al. \(2015\)](#) SDSS group catalogue. From the discussions in the above paragraphs, we deduce that perhaps the difference is inherently linked to the construction of Y07 group catalogue. As discussed in [Duarte & Mamon \(2015\)](#) potentially the imprecise scheme of computing the luminosity incompleteness as function of redshift during the group finding in Y07, which eventually propagates to the abundance matching technique leading to the incorrect estimate of group masses is a plausible culprit. In the future it would be interesting to see how the improvement in the halo mass measurement for Y07 group catalogue suggested in [Duarte & Mamon \(2015\)](#) influences the spatial mass segregation results.

4.4 Anti-segregation trend beyond the virial radius?

In a recent study of semi-analytic models of galaxy formation, [Contini & Kang \(2015\)](#) report an interesting claim that beyond the virial radius there is a global and significant increasing trend in stellar mass. They attribute this strange upturn to a presence of intrinsically massive and recently accreted objects at large radius. In our semi-analytic data GAMA-Mock presented in Section 3 (Figure 4) we note insignificant upturns (with gradient $\lesssim 0.02$ dex) in the satellite mass distribution beyond the virial radius. This is in clear contrast to the findings of [Contini & Kang \(2015\)](#).

4.5 A comment on some observed spurious trends

We find above that EAGLE data with $z \in (0.00, 0.14]$ and $\log[M_{200}/(h^{-1}M_{\odot})] \in (12.0, 12.5]$ shown in Figure 4(f), GAMA-Mock data with $z \in (0.22, 0.32]$ and $\log[M_{200}/(h^{-1}M_{\odot})] \in (12.0, 12.5]$ shown in Figure 4(e) etc show strange trends in a contrast to our overall observation of lack of mass segregation. In order to put the apparent significance of any single measurement into context we analyse the distribution of all line fits normalised by the estimated error. Here, we assume that all the measurements are independent, i.e., our fits are based on disjoint sub-samples. This distribution can be seen in Figure 9, which includes the slopes and their corresponding uncertainties for all the trends ($N = 132$) shown in Figures 4-7 and Figure 3 but excluding panels (a) and (b) of Figure 8.

We expect that such distribution is normal around the expected value. There are plethora of available statistical tests to identify departure of any distribution from normality - the Anderson-Darling A^2 test, the Kolmogorov-Smirnov D test, the Shapiro-Wilk W test, the Lilliefors test to name a few. Here, we only consider the first two tests. The data that significantly depart from a Gaussian distribution is expected (cf. Section 4.7.4 [Ivezić et al. 2014](#)) to have Anderson-Darling A^2 value $\gg 1$ and also, the Kolmogorov-Smirnov $D \gg 1/\sqrt{N}$. For our distribution the values these tests result are 1.16 and 0.2 respectively, which both suggest the distribution is consistent to being normal. As a consequence, any single “significant” result must be tempered by the large number of effective trials (i.e. distributions fit). Indeed, even the most extreme positive or negative trends are entirely

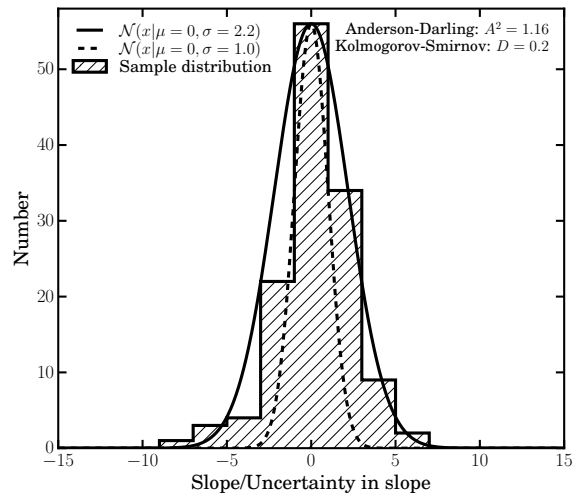


Figure 9. Distribution of the slopes of the mass segregation trend lines normalised by the estimated error. The solid and dashed lines are normal distributions with different values for dispersions overlaid for a reference.

consistent with being samples taken from this global distribution of slopes. For a reference we simply overlay a standard normal probability distribution i.e. with mean $\mu = 0$ and dispersion $\sigma = 1$, shown with the dashed line in the figure. Similarly, the smooth solid line shows a normal distribution assuming mean and dispersion of the data. Interestingly, in the figure we see that the sample distribution is broader than the standard gaussian distribution (shown with the dashed line). It means that the estimated uncertainties in the slopes in some cases could have been underestimated.

5 CONCLUSION

We investigate the controversial issue of the presence, or lack thereof, of mass segregation in galaxy groups. We provide a comprehensive study of the radial distribution of stellar mass of the satellite galaxies in galaxy groups for observations: the galaxy-redshift survey Galaxy and Mass Assembly (GAMA); semi-analytics: the GAMA lightcone mock catalogues (GAMA-Mock) constructed using a model of galaxy formation by the GALFORM group, and cosmological hydrodynamical simulation: the Evolution and Assembly of Galaxies and their Environments (EAGLE).

Overall, the absolute gradient of spatial mass segregation in galaxy groups is found to be insignificant ($\lesssim 0.04$ dex). We find this to be consistent for all the three data sets at various halo mass ranges between $12 \leq \log[M_{200}/(h^{-1}M_{\odot})] < 14.5$ and in the redshift range $0 \leq z \leq 0.32$. Analogous to the observed GAMA data, we magnitude-limit both the synthetic data i.e. GAMA-Mock and EAGLE to $r < 19.8$ mag, and carefully select stellar mass complete samples at given redshift intervals. We also find that the radial distributions of the stellar mass does not show any redshift evolution out to $z \leq 0.32$. In cases where we separate data into different redshift ranges the absolute gradients of spatial mass segregation trends were slightly larger $\lesssim 0.08$ dex but consistent to zero given the uncertainties in the slope. Moreover, we find that our results at least

for the GAMA data are robust to different halo mass and group centre estimates.

The EAGLE data give us further insights by allowing us to probe fainter magnitude limit of $r_{\text{mag}} < 22$ and also, to study the three-dimensional spatial distributions using the intrinsic stellar and virial masses. Except for the low redshift regime $z \leq 0.22$, even with the fainter magnitude limit of $r_{\text{mag}} < 22$, we find that the EAGLE data do not show any mass segregation in the halo mass range $12 \leq \log[M_{200}/(h^{-1}M_{\odot})] < 14.5$ and out to $z \leq 0.75$. This remains the case for both the projected and intrinsic data alike.

Intriguingly, the lack of mass segregation we observe is in contrast to what has recently been reported in [van den Bosch et al. \(2008\)](#); [Roberts et al. \(2015\)](#) with the SDSS group catalogues of [Yang et al. \(2007\)](#). We find that the magnitude of mass segregation seen in earlier works with SDSS group catalogues reduces when we replace their original luminosity based halo masses with dynamically inferred masses. As advocated in [Duarte & Mamon \(2015\)](#), the original estimates for halo masses from abundance matching could have propagated uncertainties from how [Yang et al. \(2007\)](#) group catalogues are constructed. A subtle effect due to using halo based group finding instead of FoF based finding could also potentially result in observed mass segregation. Interestingly, our analysis based on the SDSS group catalogue of [Saulder et al. \(2015\)](#), which uses a similar group-finder to [Robotham et al. \(2011\)](#), accompanied with implied dynamical halo masses, confirms the lack of significant evidence of mass segregation in low redshift galaxy groups. This is entirely consistent with our findings from GAMA, GAMA-Mock and EAGLE group studies and with the conclusion of [Wetzel et al. \(2012\)](#) using a revised SDSS group catalogue.

The apparent lack of mass segregation in groups suggests that whatever processes might enhance the effect (e.g. dynamical friction, mergers etc) is sub-dominant compared to competing and masking processes (e.g. long time-scales, star-formation, quenching etc).

ACKNOWLEDGEMENTS

PRK is funded through Australian Research Council (ARC) grant DP140100395 and the University of Western Australia Research Collaboration Award PG12104401 and PG12105203. PRK thanks Christoph Saulder for making the SDSS group catalogue available before the publication, and Sanjib Sharma and Weiguang Cui for discussions at earlier stages of this project. We also like to thank the referee for the comments that helped to improve the content of the paper.

GAMA is a joint European-Australasian project based around a spectroscopic campaign using the Anglo-Australian Telescope. The GAMA input catalogue is based on data taken from the Sloan Digital Sky Survey and the UKIRT Infrared Deep Sky Survey. Complementary imaging of the GAMA regions is being obtained by a number of independent survey programs including GALEX MIS, VST KiDS, VISTA VIKING, WISE, Herschel-ATLAS, GMRT and ASKAP providing UV to radio coverage. GAMA is funded by the STFC (UK), the ARC (Australia), the AAO,

and the participating institutions. The GAMA website is <http://www.gama-survey.org/>

We acknowledge the Virgo Consortium for making their simulation data available. The EAGLE simulations were performed using the DiRAC-2 facility at Durham, managed by the ICC, and the PRACE facility Curie based in France at TGCC, CEA, Bruyeres-le-Chatel.

To construct the GAMA-Mock the DiRAC Data Centric system at Durham University, operated by the Institute for Computational Cosmology on behalf of the STFC DiRAC HPC Facility (www.dirac.ac.uk), was used. This equipment was funded by BIS National E-infrastructure capital grant ST/K00042X/1, STFC capital grant ST/H008519/1, and STFC DiRAC Operations grant ST/K003267/1 and Durham University. DiRAC is part of the National E-Infrastructure. The development of the GAMA-Mock was supported by a European Research Council Starting grant (DEGAS-259586) and the Royal Society.

REFERENCES

- Abell G. O., 1958, *ApJS*, **3**, 211
- Allison R. J., Goodwin S. P., Parker R. J., de Grijs R., Portegies Zwart S. F., Kouwenhoven M. B. N., 2009, *ApJ*, **700**, L99
- Bahé Y. M., et al., 2016, *MNRAS*, **456**, 1115
- Baldry I. K., et al., 2010, *MNRAS*, **404**, 86
- Baldry I. K., et al., 2012, *MNRAS*, **421**, 621
- Balogh M. L., et al., 2014, *MNRAS*, **443**, 2679
- Beers T. C., Flynn K., Gebhardt K., 1990, *AJ*, **100**, 32
- Behroozi P. S., Conroy C., Wechsler R. H., 2010, *ApJ*, **717**, 379
- Behroozi P. S., Wechsler R. H., Conroy C., 2013, *ApJ*, **770**, 57
- Bekki K., 2009, *MNRAS*, **399**, 2221
- Berlind A. A., Weinberg D. H., 2002, *ApJ*, **575**, 587
- Berlind A. A., et al., 2006, *ApJS*, **167**, 1
- Bonnell I. A., Davies M. B., 1998, *MNRAS*, **295**, 691
- Bonnell I. A., Bate M. R., Clarke C. J., Pringle J. E., 1997, *MNRAS*, **285**, 201
- Boselli A., Gavazzi G., 2006, *PASP*, **118**, 517
- Brainerd T. G., Blandford R. D., Smail I., 1996, *ApJ*, **466**, 623
- Bryant J. J., et al., 2015, *MNRAS*, **447**, 2857
- Bullock J. S., Wechsler R. H., Somerville R. S., 2002, *MNRAS*, **329**, 246
- Carlberg R. G., et al., 1997a, *ApJ*, **476**, L7
- Carlberg R. G., et al., 1997b, *ApJ*, **485**, L13
- Cole S., Lacey C. G., Baugh C. M., Frenk C. S., 2000, *MNRAS*, **319**, 168
- Conroy C., Wechsler R. H., Kravtsov A. V., 2006, *ApJ*, **647**, 201
- Contini E., Kang X., 2015, preprint, ([arXiv:1503.08342](https://arxiv.org/abs/1503.08342))
- Cooray A., 2006, *MNRAS*, **365**, 842
- Crain R. A., et al., 2015, *MNRAS*, **450**, 1937
- De Lucia G., Kauffmann G., Springel V., White S. D. M., Lanzoni B., Stoehr F., Tormen G., Yoshida N., 2004, *MNRAS*, **348**, 333
- Diaferio A., Ramella M., Geller M. J., Ferrari A., 1993, *AJ*, **105**, 2035
- Diemand J., Moore B., Stadel J., 2004, *MNRAS*, **352**, 535
- Driver S. P., et al., 2011, *MNRAS*, **413**, 971
- Driver S. P., Davies L. J., Meyer M., Power C., Robotham A. S. G., Baldry I. K., Liske J., Norberg P., 2015, preprint, ([arXiv:1507.00676](https://arxiv.org/abs/1507.00676))
- Duarte M., Mamon G. A., 2014, *MNRAS*, **440**, 1763
- Duarte M., Mamon G. A., 2015, *MNRAS*, **453**, 3848
- Einasto J., Saar E., Kaasik A., Chernin A. D., 1974, *Nature*, **252**, 111
- Eke V. R., et al., 2004, *MNRAS*, **348**, 866

- Farrow D. J., et al., 2015, *MNRAS*, **454**, 2120
- Furlong M., et al., 2015a, preprint, ([arXiv:1510.05645](#))
- Furlong M., et al., 2015b, *MNRAS*, **450**, 4486
- Gao L., De Lucia G., White S. D. M., Jenkins A., 2004, *MNRAS*, **352**, L1
- Geller M. J., Huchra J. P., 1983, *ApJS*, **52**, 61
- Gonzalez-Perez V., Lacey C. G., Baugh C. M., Lagos C. D. P., Helly J., Campbell D. J. R., Mitchell P. D., 2014, *MNRAS*, **439**, 264
- Gunn J. E., Gott III J. R., 1972, *ApJ*, **176**, 1
- Guo Q., White S., Li C., Boylan-Kolchin M., 2010, *MNRAS*, **404**, 1111
- Guo Q., White S., Angulo R. E., Henriques B., Lemson G., Boylan-Kolchin M., Thomas P., Short C., 2013, *MNRAS*, **428**, 1351
- Guzik J., Seljak U., 2002, *MNRAS*, **335**, 311
- Han J., et al., 2015, *MNRAS*, **446**, 1356
- Hearin A. P., Zentner A. R., Berlind A. A., Newman J. A., 2013, *MNRAS*, **433**, 659
- Hickson P., 1982, *ApJ*, **255**, 382
- Hogg D. W., Bovy J., Lang D., 2010, preprint, ([arXiv:1008.4686](#))
- Hopkins A. M., et al., 2013, *MNRAS*, **430**, 2047
- Huchra J. P., Geller M. J., 1982, *ApJ*, **257**, 423
- Ivezić Ž., Connelly A. J., VanderPlas J. T., Gray A., 2014, Statistics, Data Mining, and Machine Learning in Astronomy
- Knobel C., et al., 2009, *ApJ*, **697**, 1842
- Knobel C., et al., 2012, *ApJ*, **753**, 121
- Lacey C. G., et al., 2015, preprint, ([arXiv:1509.08473](#))
- Lagos C. d. P., et al., 2015, *MNRAS*, **452**, 3815
- Le Brun A. M. C., McCarthy I. G., Schaye J., Ponman T. J., 2014, *MNRAS*, **441**, 1270
- Liske J., et al., 2015, *MNRAS*, **452**, 2087
- Ludlow A. D., Navarro J. F., Springel V., Jenkins A., Frenk C. S., Helmi A., 2009, *ApJ*, **692**, 931
- Mahdavi A., Geller M. J., Böhringer H., Kurtz M. J., Ramella M., 1999, *ApJ*, **518**, 69
- McAlpine S., et al., 2015, preprint, ([arXiv:1510.01320](#))
- McIntosh D. H., Zabludoff A. I., Rix H.-W., Caldwell N., 2005, *ApJ*, **619**, 193
- Merson A. I., et al., 2013, *MNRAS*, **429**, 556
- Moffett A. J., et al., 2016, *MNRAS*, **457**, 1308
- Moore B., Katz N., Lake G., Dressler A., Oemler A., 1996, *Nature*, **379**, 613
- Moster B. P., Somerville R. S., Maubetsch C., van den Bosch F. C., Macciò A. V., Naab T., Oser L., 2010, *ApJ*, **710**, 903
- Mulchaey J. S., 2000, *ARA&A*, **38**, 289
- Nurmi P., et al., 2013, *MNRAS*, **436**, 380
- Parker L. C., Hudson M. J., Carlberg R. G., Hoekstra H., 2005, *ApJ*, **634**, 806
- Postman M., Geller M. J., 1984, *ApJ*, **281**, 95
- Presotto V., et al., 2012, *A&A*, **539**, A55
- Reed D., Governato F., Quinn T., Gardner J., Stadel J., Lake G., 2005, *MNRAS*, **359**, 1537
- Roberts I. D., Parker L. C., Joshi G. D., Evans F. A., 2015, *MNRAS*, **448**, L1
- Robotham A. S. G., Obreschkow D., 2015, *Publ. Astron. Soc. Australia*, **32**, e033
- Robotham A., et al., 2010, *Publ. Astron. Soc. Australia*, **27**, 76
- Robotham A. S. G., et al., 2011, *MNRAS*, **416**, 2640
- Rose J. A., 1977, *ApJ*, **211**, 311
- Saulder C., van Kampen E., Mieske S., Zeilinger W. W., 2015, preprint, ([arXiv:1511.05856](#))
- Schaye J., et al., 2015, *MNRAS*, **446**, 521
- Schneider P., 2006, Extragalactic Astronomy and Cosmology
- Sheldon E. S., et al., 2004, *AJ*, **127**, 2544
- Skibba R. A., van den Bosch F. C., Yang X., More S., Mo H., Fontanot F., 2011, *MNRAS*, **410**, 417
- Springel V., et al., 2005, *Nature*, **435**, 629
- Springel V., et al., 2008, *MNRAS*, **391**, 1685
- Taylor E. N., et al., 2011, *MNRAS*, **418**, 1587
- Tempel E., et al., 2014, *A&A*, **566**, A1
- Tinker J. L., Weinberg D. H., Zheng Z., Zehavi I., 2005, *ApJ*, **631**, 41
- Tinker J. L., et al., 2012, *ApJ*, **745**, 16
- Trayford J. W., et al., 2015, *MNRAS*, **452**, 2879
- Viola M., et al., 2015, *MNRAS*, **452**, 3529
- Weigel A. K., Schawinski K., Bruderer C., 2016, preprint, ([arXiv:1604.00008](#))
- Wetzel A. R., Tinker J. L., Conroy C., 2012, *MNRAS*, **424**, 232
- White S. D. M., 1977, *MNRAS*, **179**, 33
- Yang X., Mo H. J., van den Bosch F. C., 2003, *MNRAS*, **339**, 1057
- Yang X., Mo H. J., van den Bosch F. C., Pasquali A., Li C., Barden M., 2007, *ApJ*, **671**, 153
- York D. G., et al., 2000, *AJ*, **120**, 1579
- Zheng Z., et al., 2005, *ApJ*, **633**, 791
- Ziparo F., et al., 2013, *MNRAS*, **434**, 3089
- van den Bosch F. C., Pasquali A., Yang X., Mo H. J., Weinmann S., McIntosh D. H., Aquino D., 2008, preprint, ([arXiv:0805.0002](#))
- van den Bosch F. C., Jiang F., Campbell D., Behroozi P., 2016, *MNRAS*, **455**, 158

APPENDIX A: EFFECT OF STELLAR MASS COMPLETENESS LIMITS

Here, we investigate the effect of stellar mass completeness limits in the mass segregation profiles of the GAMA data. As discussed in Section 2.4.5, we make an attempt to use a volume complete sample throughout our analysis. For this we estimate a lower stellar mass limit using the running 90th percentile of the stellar mass distribution at all redshifts for the GAMA data. But the veracity of the choice of 90th percentile can be questioned. Therefore, in Figure A1 we show the impact of our choice of the percentiles in the mass segregation trends in GAMA data in all the three redshift ranges namely $0 < z \leq 0.14$ (left panel), $0.14 < z \leq 0.22$ (mid-panel) and $0.22 < z \leq 0.32$ (right panel). The green and blue lines represent the two most massive halo mass bins. We show only the most massive halo mass bins as they are the only cases where we still have enough galaxies left in each radial and redshift bins even for an extreme choice of the stellar mass limits. The solid, dotted and dashed lines show mass segregation trends in the GAMA data with stellar mass limit estimated at the 90th, 75th and 50th percentiles of the distribution respectively. We find that the slopes of all the shown trends are $\lesssim 0.5$ and consistent with zero gradient given the uncertainties. It suggests that our adopted set of stellar mass limits as a function of redshift provides a reasonable compromise between sample completeness and sample size.

This paper has been typeset from a \LaTeX file prepared by the author.

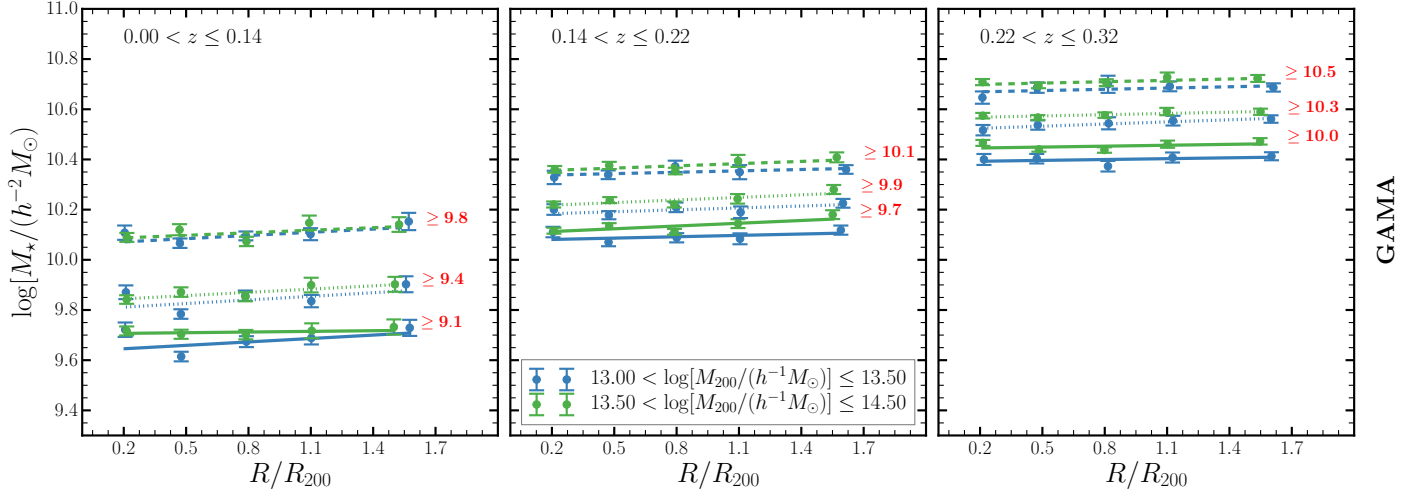


Figure A1. Effect of stellar mass completeness limits on GAMA data at three different redshift ranges, namely $0 < z \leq 0.14$ (left panel), $0.14 < z \leq 0.22$ (mid-panel) and $0.22 < z \leq 0.32$ (right panel) in the two most massive halo mass bins. The red texts shown alongside the mass segregation trends are the corresponding stellar mass limits applied to each sub-sample.